Journal Pre-proof

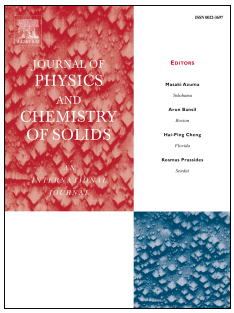

Enhanced optical properties of Cd–Mg-co-doped ZnO nanoparticles induced by low crystal structure distortion

Onyekachi Kalu, Maria R. Correia, Andrés Cantarero, Harby Alexander Martinez Rodriguez, José Alberto Duarte Moller, A. Reyes-Rojas

PII: S0022-3697(20)30210-9

DOI: https://doi.org/10.1016/j.jpcs.2020.109611

Reference: PCS 109611

To appear in: *Journal of Physics and Chemistry of Solids*

Received Date: 25 January 2020

Revised Date: 4 June 2020

Accepted Date: 5 June 2020

Please cite this article as: O. Kalu, M.R. Correia, André. Cantarero, H.A. Martinez Rodriguez, José.Alberto. Duarte Moller, A. Reyes-Rojas, Enhanced optical properties of Cd–Mg-co-doped ZnO nanoparticles induced by low crystal structure distortion, *Journal of Physics and Chemistry of Solids* (2020), doi: https://doi.org/10.1016/j.jpcs.2020.109611.

Enhanced optical properties of Cd–Mg-co-doped ZnO nanoparticles induced by low crystal structure distortion

Onyekachi Kalu [a, b, e], Maria R. Correia [d], Andrés Cantarero [b], Harby Alexander Martinez Rodriguez [a, f], José Alberto Duarte Moller [c], A. Reyes-Rojas [a]*

[a]Centro de Investigación en Materiales Avanzados, S.C., Miguel de Cervantes 120, Complejo Industrial Chihuahua, 31109 Chihuahua, CHIH, Mexico

[b]Institut de Ciencia Molecular, Universitat de València, Catedratic Jose Beltran 2, 46980 Paterna, Valencia, Spain

[c]Facultad de Ingenieria Civi, Mecánica e Industrial, Universidad de La-Salle Bajío, Av. Universidad 602, Lomas del Campestre, 37150 León, GTO, Mexico

[d]Departamento de Física, Universidade de Aveiro, Campus Universitario de Santiago, 3810-193 Aveiro, Portugal

[e]Department of Physics, Federal University of Lafia, P.M.B. 146, Lafia, Nasarawa State. Nigeria

[f]Grupo de Propiedades Térmicas, Dieléctricas de Compositos, Departamento de Ingeniería eléctrica, electrónica y computación, Universidad Nacional de Colombia, 170003 Manizales, Colombia

Abstract

The growth of $Cd_xMg_{0.125-x}Zn_{0.875}O$ nanoparticles with yellow-orange luminescence is achieved up to 2.5 at. % Cd via a modified sol–gel process. X-ray diffraction analysis confirmed that all the nanoparticles have the hexagonal wurtzite structure. It is found that Cd doping has a considerable effect on the crystal size, microstrain, band gap, and photoluminescence of the $Mg_{0.125}Zn_{0.875}O$ structure, originating from a preferred crystallographic orientation along the (101) plane of the wurtzite structure. The shift and broadening of the E_2(high) mode observed in the Raman spectra due to growth-induced strain corroborates the small distortion observed in the X-ray diffraction data. The optical band gap varies from 3.21 eV to 2.74 eV, being redshifted

with increasing Cd concentration (from 0 at. % to 2.5 at. %). The photoluminescence obtained with an excitation wavelength of 325 nm has a broad yellow-orange emission peak at around 640 nm due to transitions related to oxygen vacancies and interstitial oxygen atoms. We located the yellow-orange emission in the chromaticity coordinate diagram in the 2683–2777 K colour temperature region, demonstrating that $Cd_xMg_{0.125-x}ZnO_{0.875}$ nanoparticles have potential applications in white light-emitting diodes.

Keywords: CdMgZnO nanoparticles, Microstrain, Raman spectroscopy, Yellow-orange luminescence, Oxygen defects.

1 Introduction

The remarkable band gap (3.37 eV) and exciton binding energy (60 meV) of ZnO because of the photochemical stability have distinguished it as an excellent semiconductor material with exceptional luminescence properties in the ultraviolet–visible (UV–vis) region [1,2, 3]. As a unique luminescent material, it has novel applications in UV detectors, photodiodes, light-emitting diodes (LEDs), laser diodes, sensors, and other heterojunction and electroluminescence devices [4, 5, 6]. The detection of near-band-edge (NBE) emission at room temperature in the UV region and the broad deep-level emission (DLE) spectrum associated with defects created in the band gap are typical characteristics of the ZnO photoluminescence (PL). According to Raji et al. [7], the origin of the emission due to defect states remains unclear and controversial, and different authors relate different kinds of defects to ZnO emissions [8, 9]. However, it is widely believed that the green and red emission are related to the presence of oxygen vacancies [10] and interstitial zinc atoms, respectively [11], while the scarcely yellow-orange and orange-red emission are related to the excess of oxygen from an oxygen-rich system or atmosphere [12].

Depending on the type and amount of dopant, recent research articles and results from different authors demonstrated that dopants can modify the microstructure and influence the luminescence properties of ZnO nanostructures [13]. Among these dopants, Co^{2+}, Cd^{2+}, and Ca^{2+} have been associated with red emission [8, 14, 15], Ni^{2+}, Mn^{2+}, and Mg^{2+} have been associated with green emission [16, 17, 18,], Cu^{2+} has been associated with blue emission [19], Al^{3+} has been associated with orange-red emission [20], and p-type Si/ZnO nanostructures have been

associated with yellow-orange emission [21]. To contribute to clarification of those structure/optical interactions, we synthesized Cd–Mg-co-doped ZnO nanoparticles (NPs) by a modified sol–gel method to study the relationship between crystal structure defects and optical properties when the maximum Cd concentration is reached.

With regard to the synthesis process and photoelectronic applications of these luminescent materials, co-doping with divalent (Cd and Mg) elements is an effective technique for engineering the intrinsic defects of ZnO to turn it into an ideal luminescent material [22].

Quite obviously Mg doping widens the band gap of ZnO nanostructures, whose strong Mg–O binding energy (393.7 kJ mol^{-1}) together with good textural properties and high thermal/surface stability can control and decrease the number of irradiative centres and quench the PL coming from the surface of the nanostructures [13, 23, 24, 25]. The modulation of the electronic band gap and the red shift of the absorption edge depend on the amount of Cd doping, which is related to the broadband emission in the visible region [13,26].

However, with regard to the compositions of Cd–Mg-co-doped ZnO presented in this work, study of the role of divalent elements as dopants will provide better insight into the luminescence properties for the use of Cd–Mg-co-doped ZnO as potential material for solid-state lighting devices. Indeed, with the correct concentration of divalent elements inducing a low distortion in the crystal structure (monovalent–divalent wurtzite structure), a wide range of colour displays with enhanced visible luminescence are envisaged [27].

For the preparation of Cd–Mg-co-doped ZnO NPs, we used the method reported by Kalu et al [13], modified by use of an acetate reactant at 2.5% Cd compared with the nitrate salt reagent of only 2% reported in our previous work. Using this approach, we found that the yellow-orange PL intensity with broadband emission in the visible region depended on the Cd concentration, and the origin of the emission peak in the visible region is related to the transition from the conduction band to oxygen defects, as discussed later.

In addition, we also report the effect of increasing Cd doping on the E_2(high) mode, which is assigned to oxide vibrations that could similarly be influenced by the amount of defects without losing their crystal symmetry. We will return to this point in the discussion.

2. Experimental

$Cd_xMg_{0.125-x}ZnO_{0.875}$ NPs in the range size from 48 nm to 67 nm and with Cd atomic content from 0 to 2.5% were synthesized via a modified Pechini sol–gel technique. To prepare 0.182 mol of $Cd_xMg_{0.125-x}ZnO_{0.875}$, we started with 0.0514 mol of magnesium acetate tetrahydrate ($Mg(CH_3CO_2)_2 \cdot 4H_2O$) and 0.0323 mol of cadmium acetate dihydrate ($Cd(CH_3CO_2)_2 \cdot 2H_2O$) added to 0.0983 mol of zinc acetate monohydrate ($Zn(CH_3CO_2)_2 \cdot 2H_2O$) as Cd–Mg-co-doped ZnO metal precursors with 155 mL of distilled water under prolonged stirring. Then 0.2760 mol of the complexing agent ammoniated ethylenediaminetetraacetic acid ($C_{10}H_{16}N_2O_8$) and 0.2751 mol of citric acid monohydrate ($C_6H_8O_7 \cdot H_2O$) solution, 20 mL each, were added dropwise to the Cd–Mg-co-doped ZnO metal precursor. This solution was heated for 2 h at 65 °C with continuous stirring on a thermal bath covered with a watch glass. The transparent gel obtained was dried at 200 °C and subsequently annealed at 750 °C at a heating rate of 5 °C/min for 2 h. All reagents were of analytical grade, purchased from Sigma-Aldrich, without any further purification

2.1. Characterization

X-ray powder diffraction measurements were performed with a Bruker diffractometer (model D8 Advance) with Cu Kα (λ = 1.5405 Å) radiation operating at a voltage of 40 kV and a current of 30 mA at room temperature. The morphology of the NPs was analysed with a JEOL JEM-2200FS high-resolution transmission electron microscope operating at 200 kV with a field-emission gun and an omega filter, while the energy-dispersive X-ray spectroscopy (EDS) spectra were acquired with a Hitachi SU 3500 scanning electron microscope. UV–vis absorption spectra were recorded in the 200–800 nm wavelength range with a UV–vis–near infrared Evolution 220 spectrophotometer in diffuse reflectance mode. The Raman and PL measurements at room temperature were performed on the synthesized powder samples with use of an NTEGRA Spectra II NT-MDT atomic force microscopy–Raman system, a Jobin Yvon-Horiba T6400 triple spectrometer (with gratings of 1800 grooves per millimetre), and a Jobin Yvon HR800 spectrometer, always in backscattering geometry. The spectra were recorded with a micro-Raman setup with 532 nm excitation (second harmonic of a yttrium aluminium garnet laser) for the Raman spectra and 325 nm radiation from a He–Cd laser for the PL spectra.

3. Results and discussion

3.1. Structural characterization by X-ray diffraction

Fig. 1(a) shows the Rietveld refinement of the X-ray diffraction (XRD) patterns of $Cd_xMg_{0.125-x}ZnO_{0.875}$ (x = 0, 0.010, 0.015, 0.020, 0.025) performed with TOPAS (from Brucker). The series of diffraction peaks and their corresponding Miller indices match a hexagonal wurtzite structure belonging to ZnO (JCPDS card no. 36-1451). Also, the lack of evidence of an impurity peak associated with CdO validates that the synthesized $Cd_xMg_{0.125-x}ZnO_{0.875}$ NPs are highly crystalline with the hexagonal wurtzite phase [28, 29]. In other words, Cd incorporated in the lattice does not form CdO clusters. With increase of Cd doping up to 2.5%, although the hexagonal symmetry is preserved, a small distortion in the lattice due to the tensile stress along the [101] crystallographic direction is produced. Rietveld refinement was performed with the least-squares values based on space group $P6_3mc$, symmetry number 186 of the International Tables for Crystallography [30], and Z=2 molecules per cell, the cations and anions being at the 2b Wyckoff positions [30].

The crystallographic parameters extracted from the Rietveld fitting are given in Table 1. With increasing x, the a and c lattice parameters increase gradually from 3.2562 (1) Å to 3.2629 (2) Å and from 5.1977 (1) Å to 5.2106 (2) Å, respectively. This increase can be explained basically by the volume increase due to the larger ionic radius of Cd^{2+}(IV) (≈0.78 Å) as compared with Zn^{2+}(IV) (≈0.60 Å) [13]. The unit-cell volume (the volume of the wurtzite unit cell is given by $\sqrt{3}a^2c/8$) increase for x = 0.025 by a factor of 1.0078, while the increase due to the larger ionic radius is a factor of 1.0075. The inset in Fig. 1(a) shows the small shift produced in the (102) reflection to a lower 2θ angle when the Cd^{2+} content is increased, which gives rise to the small lattice distortion.

The effect of the microstrain observed in Table 1 (or the inset in Fig. 1(a)) can be studied by Williamson–Hall analysis [31], which relates the peak shift and broadening to the variation of the particle size and the induced lattice strain through the equation

$$\beta_{hkl}\cos\theta = \lambda/D + 4\varepsilon\sin\theta, \qquad (1)$$

where β_{hkl} is the full width at half maximum of the peak, D is the average crystallite size, ε is the average estimated microstrain, θ is the Bragg angle, and λ is the XRD wavelength previously defined.

According to this analysis, increasing values of the microstrain are related to the increasing level of Cd doping, which translates to structural distortion or defects, which contributed to the band-

gap redshift and the increasing intensity of the DLE. Furthermore, the observed positive trend shown in the graph in Fig. 1(b) (left scale) suggests a smaller lattice mismatch coming from the strain field as grain boundary defects on the addition of Cd^{2+} ions. The straight line corresponding to the evolution of the strain with the Cd content corresponds to an isotropic crystal. However, the right scale in Fig. 1(b) indicates that the crystallite size is not proportional to the strain (of course there is no reason for it to be proportional), but rather increases monotonically. This indicates an improvement of the crystalline nature of the alloy. The number of vacancies or dislocations, defects in general, may decrease [32]. The growth of the crystallite became faster when the Cd content approached 2.5%, with Cd occupying the equivalent crystallographic positions of Zn^{2+}(IV) in the tetrahedral site of the wurtzite lattice, thereby inducing a uniform state of stress with a tensile component quasiparallel to the [101] direction, which may be attributed to the increase of the unit-cell volume [33]. Clearly, a minimal increase of the unit-cell volume and the basal bond angle from 110.5° to 111.05° preserved the monovalent nanostructure of $Cd_xMg_{0.125-x}ZnO_{0.875}$. This is crucial for the PL properties because of the slightly delocalized charges around the sample on the substitution of Cd^{2+}(IV) (≈0.78 □) compared with the actual tetrahedral angle of 109.5° for Zn^{2+}(IV) (≈0.60 □).

3.2. Transmission electron microscopy and EDS analysis

Fig. 2(a) and (b) shows transmission electron microscopy images of $Cd_xMg_{0.125-x}ZnO_{0.875}$ NPs, with Fig. 2(a) corresponding to the sample grown without Cd (x = 0) and Fig. 2(b) corresponding to the sample with the highest Cd concentration (x = 0.025). From the micrographs, the sample without Cd had a nearly spherical shape, with less agglomeration and smaller grain size compared with the more agglomerated sample, with larger grain size as a consequence of the improvement of the crystallinity due to the incorporation of Cd (x = 0.025). The presence of the agglomeration with roughness and the formation of clusters could be related to the rate of reaction, dopant ion concentration in the host lattice, and possibly the duration of the annealing process leading to coalescence, which increases the particle size. An increase in the average particle size with increasing Cd content was observed after we had fit the histograms using the log-normal function, and the average particle sizes were 47.61±0.33 nm and 56.15±0.38 nm, respectively, as shown in Fig. 2(c) and (d).

As shown in Fig. 2(e) and (f), the emission peaks in the EDS spectra confirm the presence of Zn, O, Mg, and Cd at approximately 1.60 at. %. In all the spectra, the emission peaks were identified at 0.523 keV, 1.019 keV, 1.254 keV, and 3.134 keV together with additional peaks at 3.317 keV, 8.639 keV, and 9.572 keV. Among those peaks, the X-ray energies of 0.523 keV and 1.254 keV correspond to the K shell of O and Mg, while those of 1.012 keV and 3.134 keV correspond to the L-shell edge of Zn and Cd, respectively [34]. The highest emission intensity, at 1.012 keV, is attributed to the convolution of the Zn $2p_{1/2}$ and Zn $2p_{3/2}$ signals [35], while the emission with the lowest intensity, at around 3.134 keV, may correspond to the Cd $2p_{3/2}$ signal [36]. The additional X-ray emissions at 1.254 keV and 9.456 keV are assigned to the 1*s* core level of Mg and Zn, respectively, while the EDS mapping of $Cd_xMg_{0.125-x}ZnO_{0.875}$ NPs shown in Fig. 2(g)–(j) revealed a uniform distribution of Zn and O compared with that of Mg and Cd at a lower density and with the lowest atomic percentage of Cd as expected.

3.3. Optical properties of NPs

The optical absorption spectra of $Cd_xMg_{0.125-x}ZnO_{0.875}$ NPs obtained by diffuse reflectance are shown in Fig. 3(a). According to Fig. 3(a), the fundamental absorption edge at room temperature for $x = 0$ was located at 378 nm (3.21 eV), and with increasing Cd concentration the absorption edge redshifted monotonically (linearly in the $x = 0.010$–0.025 region). The UV NBE emission at 378 nm is widely known and is related to excitonic recombination of electrons from the conduction band to the valence band [24], while the redshift of the absorbance at 445 nm (2.74 eV) could be due to the presence of defects induced by the tensile strain, deep levels, or the presence of impurity states below the conduction band due to the Cd doping [37]. The redshift of the absorption edge caused by Cd (reduction in the band gap) is probably due to the low distortion of the crystal lattice that modulated the electronic structure. Furthermore, on substitution of Cd, the *s* states of the conduction band minimum can be modulated downward because of the decreasing order of the *s* states, which is 3*s* (Mg) > 4*s* (Zn) >5*s* (Cd), from the constituent atoms, thus modifying the band gap of the $Cd_xMg_{0.125-x}ZnO_{0.875}$ NPs to lower energy. Analysis of the optical band gap was performed by conversion of the diffuse reflectance spectra with the Kubelka–Munk function $F(R_\infty)$ [13], and represented by the following equations:

$$F(R_\infty) = K/S = (1 - R_\infty)^2/2R_\infty, \quad (2)$$

$$\alpha(h\nu) = A(h\nu - E_g)^m, \quad (3)$$

where R_∞ is the diffuse reflectance for a semi-infinite sample, K and S are the Kubelka–Munk absorption and scattering coefficients, α is the linear absorption coefficient of the sample, $h\nu$ is the photon energy, A is an energy-independent constant, E_g is the optical band gap, and m=½ for a direct-band-gap material.

Assuming that the sample scatters in a perfectly diffuse manner, then Tauc's formula [38] given by Eq. (3) can be written in terms of the Kubelka–Munk function as

$$[F(R_\infty)]^2 = \mathrm{B}(h\nu - E_g). \quad (4)$$

From the inset in Fig. 3(b), the relationship between the band gap and the Cd concentration shows that the $Cd_xMg_{0.125-x}ZnO_{0.875}$ NPs have a smaller band gap with increasing x. The band gaps corresponding to Cd contents x = 0, 0.01, 0.015, 0.020, and 0.025 are 3.21 eV, 2.94 eV, 2.87 eV, 2.81 eV, and 2.74 eV, respectively, as obtained from the plot of $[F(R_\infty)]^2$ versus photon energy ($h\nu$) after extrapolation of the linear portion of the energy axis to zero $F(R_\infty)$. The decreasing trend for the band gap with increasing Cd concentration was reported in our previous work [13] up to Cd content x = 0.020. Here, the band gap follows a linear decrease up to x = 0.025. This variation in the band gap can be explained on the basis of a higher concentration of carriers (Burstein shift) and the strong *p–d* interaction of the Zn 3*d* and Cd 4*d* orbitals, whose action pushes the O 2*p* orbital upward [39]. It is also obvious that the effect of Cd doping and its *d* states distorted the host lattice as already mentioned during the discussion of the XRD data, and there is an increase in the unit-cell volume leading to the redistribution of electrons and an increase of the bond length and thus a decrease in the atomic interaction [40, 41]. A stronger bond (linear combination of atomic orbitals model) produces a larger band gap. This also validates that narrowing the band gap could create sublevels (defect energy level) that are optically active as broadband emission induced by the presence of defects associated with oxygen as vacancies or interstitial atoms.

Apart from the strong effect of the *d* orbitals, the ionic strength related to metal (Mg, Zn, Cd)–oxygen (O) bonding decreases due to the replacement of Zn by Cd. This is observed as the smallest energy contribution of the *5s* orbital of Cd to the conduction band in comparison with the 3*s* and 4*s* orbitals of Mg and Zn, respectively, which moves the conduction band tail and decreases the band gap to a lower energy [42].

3.4. Raman spectroscopy

To investigate the influence of Cd doping on the composition of $Cd_xMg_{0.125-x}ZnO_{0.875}$ NPs, we performed Raman measurements; see Fig. 4(a). Normally, at the Γ (k = 0) point of the Brillouin zone, the optical phonon modes according to group theory are $A_1 + E_1 + 2B_1 + 2E_2$ for the hexagonal wurtzite lattice structure with space group $P6_3mc$ [43]. The A_1 and E_1 modes are polar phonon modes which are Raman and infrared active, the E_2 modes are nonpolar and thus are only Raman active, while the B_1 mode is a silent mode. The A_1 and E_1 polar modes split into transverse optical (TO) and longitudinal optical (LO) modes, while the two nonpolar E_2 modes are found at low (mostly the Zn atoms dominate) and high (the O movement dominates) phonon frequencies [44]. The E_1(TO) and A_1(TO) modes are first-order Raman modes, the first one arising when the zinc blende structure is folded in the c-direction to constitute the wurtzite structure. The TO–LO splitting is related to the strength of the polar bonds associated with the c-axial displacement of the cations in the lattice, the A_1(LO) and E_1(LO) modes come from the long-range electrostatic order [45, 46], while the TO modes come from deformation potential interaction [45].

The Raman spectra of $Cd_xMg_{0.125-x}ZnO_{0.875}$ for the different Cd contents (x = 0–0.025) are shown in Fig. 4(a). There are two prominent peaks: namely the E_2(low) phonon mode located at 102 cm^{-1} and the E_2(high) phonon mode located at 438 cm^{-1} for x = 0 [47], see Table 2. These modes dominate the vibrational response as cation (Cd, Mg, Zn) and oxygen components, respectively, of the synthesized NPs for x = 0 [48]. Since the E_2 modes are not polar, they are usually used to account for the stress in the material, and there is no influence of the electron concentration as in the case of the polar modes. The slight redshift of the E_2(low) mode from 102 cm^{-1} to 98 cm^{-1} and the E_2(high) mode from 438 cm^{-1} to 433 cm^{-1} as the Cd concentration increases shows the existence of a structural distortion with a good lattice mismatch in the $Cd_xMg_{0.125-x}ZnO_{0.875}$ nanostructures [49]. According to Fig. 4(b), the peak intensity of the E_2(high) mode decreases with increasing Cd concentration, which means that the incorporation of Cd gives rise to changes in the molecular environment. This observation corroborates the XRD results with increasing crystallite sizes greater than 20 nm. Also, this E_2(high) mode ascribed to oxide vibrations could be attributed to the amount of oxygen defects (oxygen vacancies or interstitial oxygen atoms) since the linear decrease in the Raman frequency of the E_2(high) phonon mode varies with increase in Cd concentration. This argument is in agreement with Ref. [50].

Furthermore, a decrease of the full width at half maximum from 18.7 cm^{-1} (x = 0) to 17.4 cm^{-1} (x = 0.025) for the E_2(high) phonon modes compared to the uniform full width at half maximum of the E_2(low) phonon mode may be attributed to shortening of the phonon lifetime initiated by a decay mechanism due to crystal defects common in doped system, hence confirming the presence of oxygen vacancies as the Cd concentration increases. Therefore, it is expected that the substitution of Cd in $Cd_xMg_{0.125-x}ZnO_{0.875}$ samples will substantially affect the size of the ordered domains and interfere with the long-range propagation of the zone centre phonons [51].

The Raman band located in the frequency region from 391 cm^{-1} to 383 cm^{-1} represents the A_1(TO) mode peak, while the small broad peaks at around 331 cm^{-1} to 326 cm^{-1} could be related to the E_2(high)–E_2(low) mode at the border of the Brillouin zone (density of states). For both Raman modes, the behaviour of the A_1(TO) and E_2(high)–E_2(low) modes suggests a monovalent lattice that is perturbed and slightly distorted from the fluctuating lattice vibration as Cd doping increases [52].

The additional modes from 513 cm^{-1} to 511 cm^{-1} and from 613 cm^{-1} to 595 cm^{-1} are assigned to the 2LA (longitudinal acoustic) and E_1(LO) scattering modes, respectively. The origin of this 2LA peak has been debated and is ascribed to a local vibrational mode due to defects, whereas the larger broadening of the E_1(LO) mode has been attributed to defects such as oxygen vacancies, interstitial zinc atoms, or defects created by Cd atoms with the in-plane atomic motion perpendicular to the *c*-axis [53]. In any case, the broadening is always increased due to disorder or lack of crystallinity.

3.5. Photoluminescence

To analyse the effect of Cd doping on the luminescence properties of $Cd_xMg_{0.125-x}ZnO_{0.875}$ NPs, the PL spectra were recorded with use of the 325 nm line of a He–Cd laser. The results are shown in Fig. 5.

We observe in Fig. 5(a) weak UV emission around 343–400 nm, in addition to a strong broad DLE [12] in the visible region. The redshift and increase in intensity of the normalized UV emission centred at 370 (±0.2) nm (3.36 eV) for x = 0.025 is shown in detail in the inset in Fig. 5(a). The slight redshift of the NBE emission peaks can be assigned to a radiative transition between the Mg 3*s*–Zn 4*s*–Cd 5*s* hybrid level and the O 2*p* level [54,55], which is the usual excitonic recombination of ZnO.

The broad visible luminescence signal spanning the range from 450 nm to 786 nm is attributed to the high-doping effect of Cd resulting in structural distortion or band gap defects as excited charge carriers recombine with impurity traps after absorbing visible light. This phenomenon shows that the formation of impurities as traps within the band gap structure (deep levels) together with a low distortion effect by Cd doping may have depleted the recombination of photogenerated charge carriers of the NBE and channelled them as strong broad emission in the entire visible spectrum of $Cd_xMg_{0.125-x}ZnO_{0.875}$, indicating the easy recombination of electrons and holes as the Cd concentration increases. Such broadband emissions corresponding to the visible region are related to DLE induced by structural defects originating from the dopants [9].

The relatively broad yellow-orange emission centred at 640 (±0.2) nm can be analysed as transitions related to interstitial oxygen atoms [21]. It is also noted that the intensity and the broadening of the linewidth of the DLE peaks increased with increasing Cd content, and this could be related to the presence of oxygen defects with induced structural distortion from the substitution of Cd, with their signatures observed as decreased intensity of the E_2(high) mode in the Raman spectrum and the increase in crystallographic parameters from the XRD results [13, 50]. A quick survey of the literature concerning the origin of yellow-orange emission attributed the emission to excess oxygen and the transitions related to interstitial oxygen atoms for ZnO nanostructures [56].

In terms of structural defects, zinc vacancies form donor–acceptor pairs with transitions associated with the broad yellow-orange emission [57], while the growth orientation along the (101) plane of the hexagonal wurtzite structure can originate from the incorporation of interstitial oxygen atoms producing the typical yellow-orange emission of Si/ZnO nanostructures according to Ref. [21]. Thus, regardless of the exact origin of the yellow-orange emission, the large ratio of the yellow-orange PL intensity to the NBE emission intensity indicates that the $Cd_xMg_{0.125-x}ZnO_{0.875}$ NPs were structurally distorted by Cd doping with a growth orientation along the (101) plane facilitating the diffusion of oxygen into the interstitial sites.

To identify the specific defects related to the broad DLE, a deconvolution of the luminescence spectra for $x = 0.025$ was performed and is shown in Fig. 5. In Fig. 5(b), the PL has been fitted with four Gaussians with their peaks positioned at 479 (±0.2) nm (≈2.58 eV), related to blue emission attributed to interstitial zinc atoms and zinc vacancies, 565 (±0.2) nm (≈2.19 eV), related to yellow emission from neutral oxygen vacancies, 644 (±0.2) nm (≈1.92 eV), related to

orange emission associated with interstitial oxygen atoms, and 709 (±0.2) nm (≈1.75 eV), related to red emission connected to interstitial oxygen atoms, donor–acceptor transitions of oxygen vacancies, and zinc vacancies. The findings of some studies reporting defects states and their luminescence properties are consistent with the deconvoluted peaks for x = 0.025 [12, 20, 22, 32,58].

In addition, it is also observed that the deconvoluted spectra were dominated by the contribution of zinc vacancies, monovalent neutral oxygen vacancies, and interstitial oxygen atoms, where the intensity of the deconvoluted spectra for yellow and orange region are dominated as the source of the yellow-orange emission of $Cd_xMg_{0.125-x}ZnO_{0.875}$ NPs.

Accordingly, to determine the exact emission colour and colour purity of the samples, the International Commission on Illumination (CIE) chromaticity diagram was calculated from the PL spectra of the samples under 325 nm excitation; the corresponding chromaticity coordinates are given in Table 3.

In Fig. 6, the chromaticity coordinates for $Cd_xMg_{0.125-x}ZnO_{0.875}$ NPs marked with triangles in the CIE 1931 chromaticity diagram were located in the yellow-orange region and thus facilitated the formation of broadband emission with low crystal distortion by Cd dopant. The correlated colour temperature (CCT), which is related to the colour appearance, was calculated with the McCamy equation [59]:

$$CCT = -449n^3 + 3525n^2 - 6823.3n + 5520.33, \quad (5)$$

where $n=(X - X_e)/(Y - Y_e)$ is the inverse slope of the line that is defined from the chromaticity epicentre given as X_e = 0.3320, Y_e = 0.1858, where X and Y are the sample chromaticity coordinates.

In Table 3, the CCTs obtained for $Cd_xMg_{0.125-x}ZnO_{0.875}$ are on the order of 2700 K. These values are close to the CCTs for soft white compact fluorescent and LED lamps, which makes $Cd_xMg_{0.125-x}ZnO_{0.875}$ a suitable material for warm white light when combined with a blue LED chip.

4. Conclusions

Single-phase $Cd_xMg_{0.125-x}ZnO_{0.875}$ NPs were synthesized by a modified sol–gel route with Cd dopant to increase the optical efficiency. Structural studies showed that the band gap narrowed to lower energies, up to 2.74 eV, with increasing Cd content. An increase in the linewidth was also

observed, and the yellow-orange emission intensity appears to increase with the amount of Cd. From the PL studies, the emerging high intensity of yellow-orange emission at 640 nm is believed to be due to the transitions associated with interstitial oxygen atoms, which reflects a structural distortion along the (101) plane of the wurtzite $Cd_xMg_{0.125-x}ZnO_{0.875}$ NPs induced by Cd doping. The CIE colour coordinates of all the samples are located in the yellow-orange region of the chromaticity diagram with low CCTs as soft white light, suggesting that $Cd_xMg_{0.125-x}ZnO_{0.875}$ NPs hold great promise in the application of low-cost white LEDs and other light devices.

Acknowledgements

The authors thank and acknowledge CONACYT (grant number 10067) and the members of staff at the Centro de Investigación en Materiales Avanzados, S.C, Mexico, for the characterization and analysis. M. Rosário Correia acknowledges the financial support of FEDER funds through the COMPETE 2020 Programme and National Funds through the Portuguese Foundation for Science and Technology under project UID/CTM/50025/2019. M. Rosário Correia thanks J. Cardoso and N. Ben Serine for great help with photoluminescence measurements.

Fig. 1. (a) Rietveld refinement of $Cd_xMg_{0.125-x}ZnO_{0.875}$ (x = 0, 0.010, 0.015, 0.020, 0.025) nanoparticles annealed at 750 °C. The inset shows the shift of the (102) reflection with Cd content (see the text).

(b) Average microstrain and crystallite size versus Cd atomic content.

Fig. 2. Transmission electron microscopy images of $Cd_xMg_{0.125-x}ZnO_{0.875}$ for x = 0 (a) and x = 0.025 (b). Histograms of particle size distribution for x = 0 (c) and x= 0.025 (d). (e,f) Energy-dispersive X-ray spectroscopy spectra of $Cd_xMg_{0.125-x}ZnO_{0.875}$ for x = 0 (e) and x = 0.025 (f). Mapping of the $Cd_xMg_{0.125-x}ZnO_{0.875}$ nanoparticles corresponding to the $L\alpha_{1-2}$ edge of Zn (g), $K\alpha_1$ of O (h), $K\alpha_{1-2}$ of Mg (i), and $L\alpha_1$ of Cd (j).

Fig. 3. (a) Optical absorption spectra and (b) $[F(R_\infty)]^2$ versus photon energy ($h\nu$) for $Cd_xMg_{0.125-x}ZnO_{0.875}$ nanoparticles.

Fig. 4. (a) Raman spectra recorded at room temperature for $Cd_xMg_{0.125-x}ZnO_{0.875}$ nanoparticles. The excitation wavelength was 532 nm. (b) Raman frequency of the E_2(high) mode for $Cd_xMg_{0.125-x}ZnO_{0.875}$ as a function of Cd concentration. LA, longitudinal acoustic; LO, longitudinal optical; TO, transverse optical.

Fig. 5. (a) Photoluminescence (PL) spectra of $Cd_xMg_{0.125-x}ZnO_{0.875}$ nanoparticles. (b) Deconvoluted PL spectra (for x= 0.025) obtained with 325 nm excitation from a He–Cd laser. Oi, interstitial oxygen atoms; V_O, oxygen vacancies, V_{Zn}, zinc vacancies.

Fig. 6. Chromaticity coordinates of $Cd_xMg_{0.125-x}ZnO_{0.875}$ (x = 0, 0.010, 0.015, 0.020, 0.025) in the CIE 1931 diagram obtained with 325 nm excitation.

Table 1. Crystallographic parameters of $Cd_xMg_{0.125-x}ZnO_{0.875}$ nanoparticles obtained from Rietveld fitting and Eq. (1).

Cd^{2+} content x	Lattice parameter a, b (Å)	c (Å)	Cell volume V (Å^3)	Crystal size D (nm)	Microstrain $\varepsilon \times 10^{-3}$	Zn–O–Zn bond angle (°)	Reliability factor χ^2
0	3.2543 (1)	5.1977 (1)	47.673 (1)	48 (1)	0.011(1)	110.09	1.27
0.010	3.2562 (1)	5.2009 (1)	47.758 (1)	52 (1)	0.100 (1)	111.01	1.78
0.015	3.2582 (1)	5.2047 (1)	47.851 (1)	53 (1)	0.141 (1)	111.02	1.77
0.020	3.2587 (1)	5.2051 (1)	47.871 (1)	55 (1)	0.151 (1)	111.04	2.09
0.025	3.2629 (2)	5.2106 (2)	48.044 (2)	67 (1)	0.189 (1)	111.05	2.21

Table 2. Phonon modes in the Raman spectra of $Cd_xMg_{0.125-x}ZnO_{0.875}$ nanoparticles.

Cd^{2+} content x	E_2(low) (cm^{-1}) (±0.1)	$E_2(high) - E_2$(low) DOS (cm^{-1}) (±0.1)	A_1(TO) (cm^{1}) (±0.1)	E_2(high) (cm^{-1}) (±0.1)	2LA (cm^{-1}) (±0.1)	E_1(LO) (cm^{-1}) (±0.1)
0	102.0	331.9	390.0	438.0	513.0	612.2
0.010	100.0	327.6	385.2	436.0	512.0	609.3
0.015	99.5	328.7	384.1	435.5	511.5	604.0
0.020	99.0	327.0	383.3	434.2	510.5	598.4
0.025	98.0	326.4	382.5	433.0	510.3	595.3

DOS, density of states; LA, longitudinal acoustic; LO, longitudinal optical; TO, transverse optical.

Table 3. CIE chromaticity coordinates, correlated colour temperature and Ra values of $Cd_xMg_{0.125-x}ZnO_{0.875}$ (x = 0, 0.010, 0.015, 0.020, 0.025) nanoparticles.

Cd^{2+} content x	CIE coordinates		Correlated colour temperature (K)	Ra
	X	Y		
0	0.4781	0.4409	2683	92
0.010	0.4799	0.4419	2668	92
0.015	0.4772	0.4386	2678	93
0.020	0.4745	0.4440	2750	92
0.025	0.4679	0.4356	2777	93

References

[1] H.A. Qayyum, M.F. Al-Kuhaili, M.A. Durrani, T. Hussain, M. Ikram, Blue shift in the optical transition of ZnO thin film due to an external electric field, J. Phys. Chem. Solids, 112 (2018) 94–99.

[2] G. Bajpai, T. Srivastava, F. Husian, S. Kumar, S. Biring, S. Sen, Enhanced red emission from Fe/Si co-doped ZnO nano-particles, Scr. Mater. 144 (2018) 27–30.

[3] M.M. Mahendiran, J.J. Mathen, M. Racik, J. Madhavan, M.V.A. Raj, Investigation of structural, optical and electrical properties of transition metal/oxide semiconductor ZnO-CdO nanocomposite and its effective role in the removal of water contaminant, J. Phys. Chem. Solids 126 (2019) 322–334.

[4] R. Zhao, K. Li, Z. Wang, X. Xing, Y. Wang, Gas-sensing performance of Cd-doped ZnO nanoparticles synthesized by a surfactant-mediated method for n-butanol gas, J. Phys. Chem. Solids 112 (2018) 43–49.

[5] S. Choudhary, Structural, optical, dielectric and electrical properties of (PEOPVP)–ZnO nanocomposites, J. Phys. Chem. Solids 121 (2018) 196–209.

[6] V. Padmavathy, S. Sanka, Tuning the Optical properties of ZnO:Cd by doping La and Y, Superlattices Microstruct. 128 (2019) 127–135.

[7] R. Raji, K.G. Gopchandran, ZnO nanostructures with tunable visible luminescence: Effects of kinetics of chemical reduction and annealing, J. Sci. Adv. Mater. Devices 2 (2017) 51–58.

[8] L. Prochazkova, V. Cuba, A. Beitlerova, V. Jary, S. Omelkov, M. Nikl, Ultrafast Zn(Cd,Mg)O:Ga nano scintillators with luminescence tunable by band gap modulation, Opt. Exp. 28(22) (2018) 29482.

[9] A. Janotti, C.G. Van de Walle, Native point defects in ZnO, Phys. Rev. B 76(16) (2007) 165202.

[10] S. Agarwal, L.K. Jangir, K.S. Rathore, M. Kumar, K. Awasthi, Morphology dependent structural and optical properties of ZnO nanostructures, Appl. Phys. A 125 (2019) 553.

[11] V. Kumar, H.C. Swart, O.M. Ntwaeaborwa, R.E. Kroon, J.J. Terblans, S.K.K. Shaat, A. Yousif, M.M. Duvenhage, Origin of the red emission in zinc oxide nanophosphors, Mater. Lett. 15 (2013) 57.

[12] A.L. Curcio, J.W. Martínez Espinosa, P.S. Pizani, A.D. Giovanni Rodrigues, Effects of cadmium insertion in blue-excited photoluminescence of ZnO, Opt Mater. 89 (2019) 344–348.

[13] O. Kalu, J.A.D. Moller, A.R. Rojas, Structural and optical properties of cadmium magnesium zinc oxide (CdMgZnO) nanoparticles synthesized by sol-gel method, Phys. Lett. A 383(10) (2019) 1037–1046.

[14] T.T. Loan, N.N. Long, L.H. Ha, Photoluminescence properties of Co-doped ZnO nanorods synthesized by hydrothermal method, J. Phys. D. Appl. Phys. 42 (2009) 06541.

[15] K. Puniaa, G. Lala, P.A. Alvib, S.N. Doliac, S. Dalelad, K.B. Modie, S. Kumara, A comparative study on the influence of monovalent, divalent and trivalent doping on the structural, optical and photoluminescence properties of $Zn_{0.96}T_{0.04}O$ (T: Li^{+}, Ca^{2+}, Gd^{3+}) nanoparticles, Ceram. Int. 45 (2019) 13473–13482.

[16] S. Fabbiyola, V. Sailaja, L.J. Kennedy, M. Bououdina, J.J. Vijaya, Optical and magnetic properties of Ni-doped ZnO nanoparticles. J. Alloy. Compd. 694 (2017) 522–531.

[17] P.S. Sundaram, S.S. Rajkumar Inbanathan, G. Arivazhagan, Structural and optical properties of Mn doped ZnO nanoparticles prepared by co-precipitation method, Physica B 574 (2019), 411668.

[18] R.C. Oliveira, D.E. Martins, M.I.B. Bernadi, A. Mesquita, $Zn_{1-x}Mg_xO$ nanoparticles prepared by the polymeric precursor method: correlation between photoluminescence and local structure, Opt. Mater. 86 (2018) 71–78.

[19] M. Ashokkumar, S. Muthukumaran, Effect of Ni doping on electrical, photoluminescence and magnetic behavior of Cu doped ZnO nanoparticles, J. Lumin. 162 (2015) 97–103.

[20] E. Musavi, M. Khanlary, Z. Khakpour, Red–orange photoluminescence emission of sol-gel dip-coated prepared ZnO and ZnO.Al nano-crystalline films, J. Lumin. 216 (2019) 116696.

[21] S. Dellis, N. Pliatsikas, N. Kalfagiannis, O. Lidor-Shalev, A. Papaderakis, G. Vourlias, S. Sotiropoulos, D.C. Koutsogeorgis, Y. Mastai, P. Patsalas, Broadband luminescence in defect-engineered electrochemically produced porous Si/ZnO nanostructures, Sci. Rep. 8 (2018) 6988.

[22] N. Tu, H. Van Bui, D.Q. Trung, A.-T. Duong, D.M. Thuy, D.H. Nguyen, K.T. Nguyen, P.T. Huy, Surface oxygen vacancies of ZnO: a facile fabrication method and their contribution to the photoluminescence, J. Alloy. Compd. 791 (2019) 722–729.

[23] S. Yizhe, J. Yibin, P. Huiren, W. Jiangliu, Z. Shengdong, C. Shuming, Efficient quantum dot light emitting diodes with a $Zn_{0.85}Mg_{0.15}O$ interfacial modification layer, Nanoscale 9 (2017) 8962.

[24] Z.J. Othman, A. Matoussi, F. Fabbri, F. Rossi, G. Salviati, Optical and structural properties of $Zn_{1-x}Mg_xO$ ceramics materials, Appl. Phys. A. 166 (2014) 1501–1509.

[25] I. Umaralikhan, M.J.M. Jaffar, Green synthesis of ZnO and Mg doped ZnO nanoparticles, and its optical properties, J. Mater. Sci. Mater. Electron. 28 (2017) 7677–7685.

[26] L.T. Jule, F.B. Dejene, A.G. Ali, K.T. Roro, A. Hegazy, N.K. Allam, E. El Shenawy, Wide visible emission and narrowing band gap in Cd-doped ZnO nanopowders synthesized via sol-gel route, J. Alloy. Compd. 687 (2016) 920–926.

[27] S.B. Woodley, A.A. Sokol, C.R.A Catlow, A.A. Al-Sunaids, S.M. Woodley, Structural and optical properties of Mg and Cd doped ZnO nanoclusters, J. Phys. Chem. C 117 (2013) 27127–27145.

[28] M. Arshad, M.M. Ansari, A.S. Ahmed, P. Tripathi, S.S. Ashraf, A.H. Naqvi, A. Azam, Bandgap engineering and enhanced photoluminescence of Mg doped ZnO nanoparticles synthesized by wet chemical route, J. Lumin. 161(28) (2015) 275–280.

[29] M.I. Aroyo, J.M. Perez-Mato, D. Orobengoa, E. Tasci, G. de la Flor, A. Kirov, Crystallography online: Bilbao Crystallographic Server, Bulg. Chem. Commun. 43(2) (2011) 183–197.

[30] M.I. Aroyo, A. Kirov, C. Capillas, J.M. Perez-Mato, H. Wondratschek, Bilbao Crystallographic Server II: representations of crystallographic point groups and space groups, Acta Crystallogr. A62 (2006) 115–128.

[31] N.S. Goncalves, J.A. Carvalho, Z.M. Lima, J.M. Sasaki, Size-strain study of NiO nanoparticles by X-ray powder diffraction line broadening, Mater. Lett. 72 (2012) 36–38.

[32] H. Zeng, G. Duan, Y. Li, S. Yang, X. Xu, W. Cai, Blue luminescence of ZnO nanoparticles based on non-equilibrium processes: defects origins and emission controls, Adv. Funct. Mater. 20(4) (2010) 561–572.

[33] J. Luo, S. Zhao, P. Wu, K. Zhan, C. Peng, S. Zheng, Synthesis and characterization of new Cd-doped ZnO/ZnS core shell quantum dot with tunable and highly visible photoluminescence, J. Mater. Chem. C 3 (2015) 3391–3398.

[34] J.C. Fuggle, N. Martensson, Core level binding energies in metals, J. Electron Spectrosc. Relat. Phenom. 21 (1980) 275.

[35] C.D. Wanger, W.M. Riggs, L.E. Davis, J.F. Moulder, G.E. Muilenberg, Handbook of X-Ray Photoelectron Spectroscopy, Perkin-Elmer, Eden Prairie, 1979.

[36] J.A. Bearden, A.F. Burr, Re-evaluation of X-ray Atomic energy levels, Rev. Mod. Phys. 39 (1967) 125.

[37] F. Wang, B. Liu, C. Zhao, S. Yuan, Synthesis of $Zn_{1-x}Cd_xO$ bramble-like Nanostructure, Mater. Lett. 63(15) (2009) 1357–1359.

[38] J. Tauc, Optical properties of amorphous semiconductors, in: J. Tauc) Ed.), Amorphous and Liquid Semiconductors, Springer, Boston, 1974, pp. 159–220.

[39] P. Schroer, P. Kriiger, J. Pollmann**,** First-principles calculation of the electronic structure of the wurtzite semiconductors Zno and ZnS, Phys. Rev. B 47(12) (1993) 6971–6980.

[40] W. Zhan, V. Venkatachalapathy, T. Aarholt, A.Y. Kuznetsov, Ø. Prytz, Band gap maps beyond the delocalization limit: correlation between optical band gaps and plasmon energies at the nanoscale, Sci. Rep. 8 (2018) 848.

[41] N. Rana, S. Chand, A.K. Gathanian, Tailoring the structure and optical properties of ZnO by doping with Cd, Ceram. Int. 41(9) (2015) 12032–12037.

[42] J.C. Phillips, Ionicity of the chemical bond in crystals, Rev. Mod. Phys. 42 (1970) 317–356.

[43] T.C. Damen, S.P. Porto, B. Tell, Raman effect in ZnO, Phys Rev. 142(2) (1966) 571–574.

[44] C.V. Reddy, B. Babu, J. Shim, Synthesis, optical and efficient photocatalytic activity of CdO/ZnO hybrid nanocomposite, J. Phys. Chem. Solids 112 (2018) 20–28.

[45] A. Cantarero, C. Trallero-Giner, M. Cardona, Excitons in one phonon Raman scattering: Fröhlich and interference effects, Phys. Rev. B 40 (1989) 12290–12295.

[46] C.A. Arguello, D.L. Rousseau, S.P. Porto, First-order Raman effect in wurtzite-type crystals, Phys Rev. 181 (1969) 1351–1363.

[47] Z.Y. Jiang, K.R. Zhu, Z.Q. Li, W.W. Jin, G. Li, Structure and Raman scattering of Mg-doped ZnO nanoparticles prepared by sol–gel method, Rare Met. 37 (2018) 881–885.

[48] W.S. Mohamed, A.M. Abu-Dief, Synthesis characterization and photocatalysis enhancement of Eu_2O_3-ZnO mixed oxide nanoparticles, J. Phys. Chem. Solids 116 (2018) 375–385.

[49] D.A. Guzmán-Embús, M.F. Vargas-Charry, C. Vargas-Hernández, Optical and structural properties of ZnO:Cd particles grown by hydrothermal method, J. Am. Ceram. Soc. 98(5) (2015) 1498–1505.

[50] S.A. Ansar, M.M. Khan, S. Kalathil, A. Nisar, J. Lee, M.H. Cho, Oxygen vacancies induced bandgap narrowing of ZnO nanostructure by electrochemically active biofilm, Nanoscale 5 (2013) 9238–9246.

[51] F. Wang, H. He, Z. Ye, L. Zhu, H. Tang, Y. Zhang, Raman scattering and Photoluminescence of quasi- aligned ternary ZnCdO nanorods, J. Phys. D Appl. Phys. 38 (2005) 2919–2922.

[52] C-J. Pan, K.F. Lin, W.T. Hsu, W.F. Hsieh, Structural and optical properties of ZnMgO nanostructures formed by Mg in diffused ZnO nanowires, J. Solid State Chem. 180 (2007) 1188–1192.

[53] J.M. Calleja, M. Cardona, Resonant Raman scattering in ZnO, Phys. Rev. B 16 (1977) 3753–3761.

[54] D.W. Ma, Z.Z. Yel, Y.S. Yan, Photoluminescent analysis of $Zn_{1-x}Cd_xO$ alloys Appl. Phys. B 82 (2006) 85–87.

[55] J. Jiang, L. Zhu, Y. Li, Y. Guo, W. Zhou, L. Cao, H. He, Z. Ye, Bandgap modulation of ZnCdO alloy thin films with different Cd content grown by pulsed laser deposition, J. Alloy. Compd. 547 (2014) 59–62.

[56] A.B. Djurisic, Y.H. Leung, K.H. Tam, L. Ding, W.K. Ge, H.Y. Chen, S. Gwo, Green, yellow, orange defect emission from ZnO nanostructures: influence of excitation wavelength, Appl. Phys. Lett. 88 (2006) 103107.

[57] R. Radoi, P. Fernández, J. Piqueras, M.S. Wiggins, J. Solis, Luminescence properties of mechanically milled and laser irradiated ZnO, Nanotechnology 14 (2003) 794–798.

[58] V. Kumar, H.C. Swart, O.M. Ntwaeaborwa, R.E. Kroon, J.J. Terblans, S.K.K. Shaat, A. Yousif, M.M. Duvenhage, Origin of the red emission in zinc oxide nanophosphors, Mater. Lett. 101 (2013) 57–60.

[59] S.C. McCamy, *Correlated color temperature as an explicit function of chromaticity coordinates*, Color Res. Appl. 17(2) (1992) 142–144.

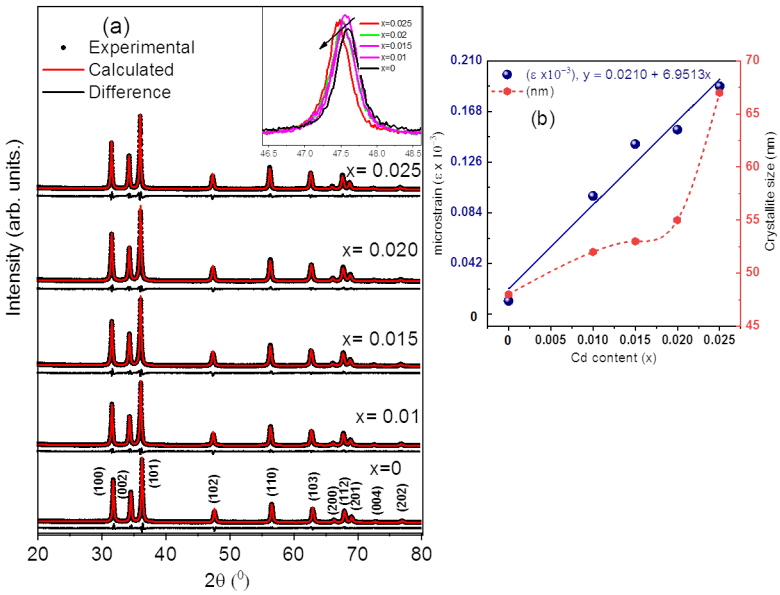

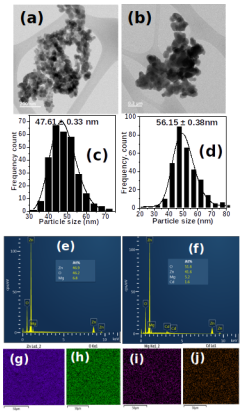

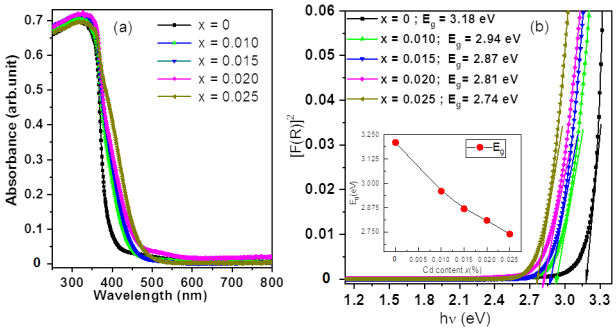

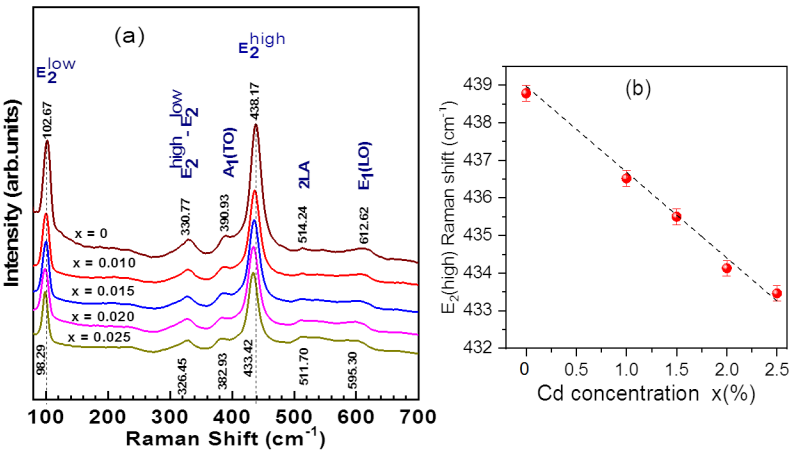

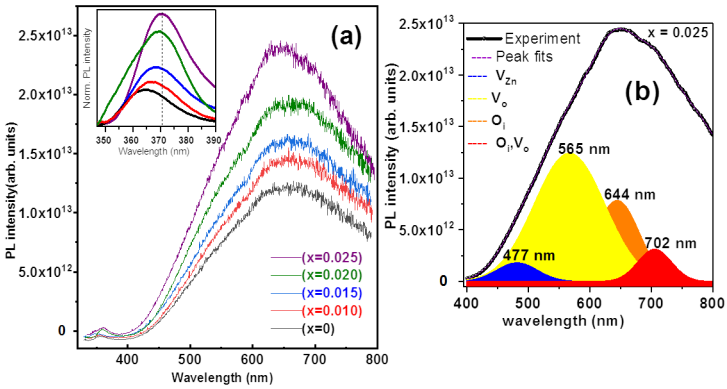

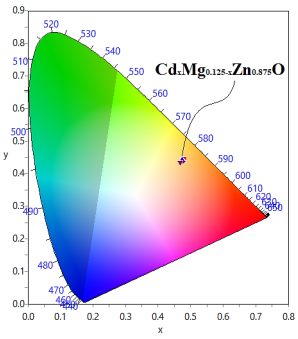

Highlights

- Enhanced optical properties induced by oxygen defects, and a structural distortion along the (101) plane of the wurtzite structure are discussed.
- Rietveld analysis and the E_2 (high) phonon mode revealed an increase in the tensile stress component with increasing Cd concentration.
- By exchange interaction of the Cd 4*d* and O 2*p* orbitals, the band gap is modified and sublevels (defect energy level) are created.
- Photoluminescence spectra show transitions associated with oxygen defects, which increase with the amount of Cd in the solid solution.

Declaration of interests

☑ The authors declare that they have no known competing financial interests or personal relationships that could have appeared to influence the work reported in this paper.

☐ The authors declare the following financial interests/personal relationships which may be considered as potential competing interests: